Available online at www.sciencedirect.com

ScienceDirect

Underground Space 27 (2026) 132–149

www.keaipublishing.com/undsp

Research Paper

Mechanical behavior of shield tunnel reinforced with corrugated plates: from joint to full ring

Yingjie Guo [a,b,c], Wenqi Ding [a,b], Chang Ma [a,b,*], Jixiang Tang [a,b], Qingzhao Zhang [a,b]

[a] Department of Geotechnical Engineering, College of Civil Engineering, Tongji University, Shanghai 200092, China
[b] Key Laboratory of Geotechnical and Underground Engineering of Ministry of Education, Tongji University, Shanghai 200092, China
[c] Shandong Provincial Communications Planning and Design Institute Group Co., Ltd., Jinan 250031, China

Received 16 November 2024; received in revised form 22 January 2025; accepted 11 March 2025
Available online 29 December 2025

Abstract

To mitigate the defects of shield tunnels in operation, a reinforcement method using corrugated plates was proposed. This paper aims to present a comprehensive investigation of the effectiveness of this method. Taking into account the corrugated plate joints, full-scale tests were designed and conducted on two specimens of segmental joints: one unreinforced and one reinforced. The test results revealed that the failure mode of the reinforced specimen was characterized by shear failure of the chemical anchors, followed by concrete crushing. The effectiveness of reinforcement highly depends on the shear capacity of the chemical anchors. After reinforcement, the flexural stiffness and ultimate bearing capacity of the specimen increased by 112.4% and 32.5%, respectively. Two refined numerical models, developed at both the joint scale and full-ring scale, were validated for corrugated plate reinforced shield tunnels. The numerical results indicated that, with full-ring reinforcement, the overall stiffness and the bearing capacity increased by 341.4% and 39.6%, respectively. Notably, shear stress in the chemical anchors was more pronounced at the tunnel vault and haunch, suggesting the need for localized optimization of the chemical anchors in these areas.

Keywords: Shield tunnel; Segmental joints; Corrugated plate reinforcement; Mechanical test; Numerical simulation

1 Introduction

Shield tunnels are inevitably exposed to complex defects over their service life, such as large deformation, segment cracking, joint dislocation, and water leakage (Li et al., 2023; Yuan et al., 2013). These issues can alter the stress distribution within the tunnel segments and adversely affect durability. Current tunnel reinforcement methods include using steel plates (Chang et al., 2001; Liu et al., 2018; Zhai et al., 2020), fiber-reinforced polymers (Liu et al., 2020; Zahran, 2016), steel–concrete composites (Zhang et al., 2019), and epoxy-bonded filament-wound profiles (Liu et al., 2017), but with some limitations, such as restricted improvement in performance or complex installation requirements (Ding et al., 2023a). Thus, identifying an efficient and effective reinforcement method is critical to ensuring the long-term safety and reliability of shield tunnels.

Corrugated plate structures were first applied to highway bridges and later extended to culverts and tunnels (Ma et al., 2024; Rauch et al., 1994). As a prefabricated structure, corrugated plates offer advantages such as high strength, installation efficiency, and cost-effectiveness, making them well-suited for tunnel maintenance (Kang & Davidson, 2013; Tetreault et al., 2018). Experimental and numerical studies have assessed the effects of corrugated plate reinforcement on shield tunnel segments and segmental joints (Ding et al., 2023a, 2023b; Ren et al., 2019). The results indicate that corrugated plate reinforcement can

* Corresponding author at: Department of Geotechnical Engineering, College of Civil Engineering, Tongji University, Shanghai 200092, China.
E-mail address: 2232263@tongji.edu.cn (C. Ma).
Peer review under the responsibility of Tongji University.

https://doi.org/10.1016/j.undsp.2025.03.008

Nomenclature

ΔD	vertical convergence of the tunnel	M	bending moment of the segmental joint
e	eccentricity of the joint section	N	horizontal load applied to the specimen
F	vertical load applied to the specimen	P_1	load group 1 in full-ring model
G	gravity of the segment	P_2	load group 2 in full-ring model
h	thickness of the segment	P_3	load group 3 in full-ring model
K_θ	flexural stiffness of the segmental joint	θ	joint rotation angle
L	horizontal distance of N to the joint section	δ_1	variation of joint opening of intrados face
L_1	horizontal distance of F to the joint section	δ_2	variation of joint closing of extrados face
L_2	horizontal distance of G to the joint section		

increase segment stiffness by 36% and bearing capacity by 201%, highlighting its exceptional reinforcing capability.

Both corrugated plate structures and shield tunnel linings are fabricated structures, with joints playing a crucial role in influencing the overall performance (Do et al., 2014). Consequently, extensive research has focused on the mechanical characteristics of segmental joints (Arnau & Molins, 2012; Wu et al., 2023) and corrugated plate joints (Mikhailovsky et al., 1992; Zhao et al., 2023). In the corrugated plate reinforced structure, the bearing performance is significantly affected by the collaborative behavior of these two types of joints. Previous studies have used an individual corrugated plate as reinforcement, neglecting the influence of the corrugated plate joint. Additionally, attention has primarily been paid to joint-scale components, with limited investigation into the effects of reinforcement on the full-ring tunnel, which holds greater practical significance for engineering applications. However, full-ring scale tests are often prohibitively costly and resource-intensive. With advancements in computational power, refined numerical models have become a viable alternative for accurately simulating structural behavior (Cao et al., 2012; Su et al., 2022).

In this study, unreinforced and reinforced specimens incorporating both segmental joints and corrugated plate joints were designed, and full-scale tests were conducted to investigate the mechanical behavior and failure modes. Subsequently, two refined numerical models, at the joint scale and full-ring scale, are developed to comprehensively explore the effects of corrugated plate reinforcement on shield tunnels.

2 Experimental study

2.1 Specimen design

The experiment was composed of two sets of full-scale specimens of shield tunnel segmental joints, designated as SP-0 and SP-1, representing unreinforced and reinforced conditions, respectively. Both specimens were identical in material and specifications, with a dimension of 2422 mm × 1200 mm × 350 mm (length × width × thickness). Each specimen was assembled from two segments joined by 5.8-graded bent bolts. The segments were cast with C50-graded concrete, and the reinforcement cage was constructed using HPB300 and HRB400 rebars. For the reinforced specimen (SP-1), corrugated plates made from S32001 stainless steel with a thickness of 6 mm were utilized. Each corrugated plate joint includes holes for special bolts and chemical anchors. The special bolts connected adjacent corrugated plates, while the chemical anchors attached the corrugated plates to the segments. The details of the specimen are illustrated in Fig. 1.

The assembly process for SP-1 is illustrated in Fig. 2. The assembly of SP-0 followed the same procedure as SP-1, except it did not include the installation of corrugated plates. The assembly steps for SP-1 are as follows:

(1) Gasket installation: Gaskets were adhered to the groove on the surface of the segmental joint.
(2) Bent bolt installation: The bent bolts were tightened using a torque wrench, aiming for a pre-tightening torque of 90 N·m.
(3) Chemical anchor hole positioning: After cleaning the surface of the segment, a 20 mm diameter drill was used to create holes for chemical anchors, with a drilling depth of 125 mm. Following drilling, a high-pressure air gun was used to clean dust from the anchor holes.
(4) Corrugated plates assembly: The corrugated plates were positioned and fixed in place using chemical anchors and special bolts.

2.2 Test apparatus and loading scheme

The experimental setup utilized the TJ-GPJ2000 loading system at the Key Laboratory of Geotechnical and Underground Engineering of the Ministry of Education in Tongji University, as shown in Fig. 3(a). The setup included three vertical actuators and four horizontal actuators. The vertical actuator transmitted force to the specimen through a distribution beam spaced 800 mm between beams. The steel supports were mounted on rollers to establish simply supported boundary conditions. The diagrams of force application are shown in Fig. 3(b) and (c). Based on force

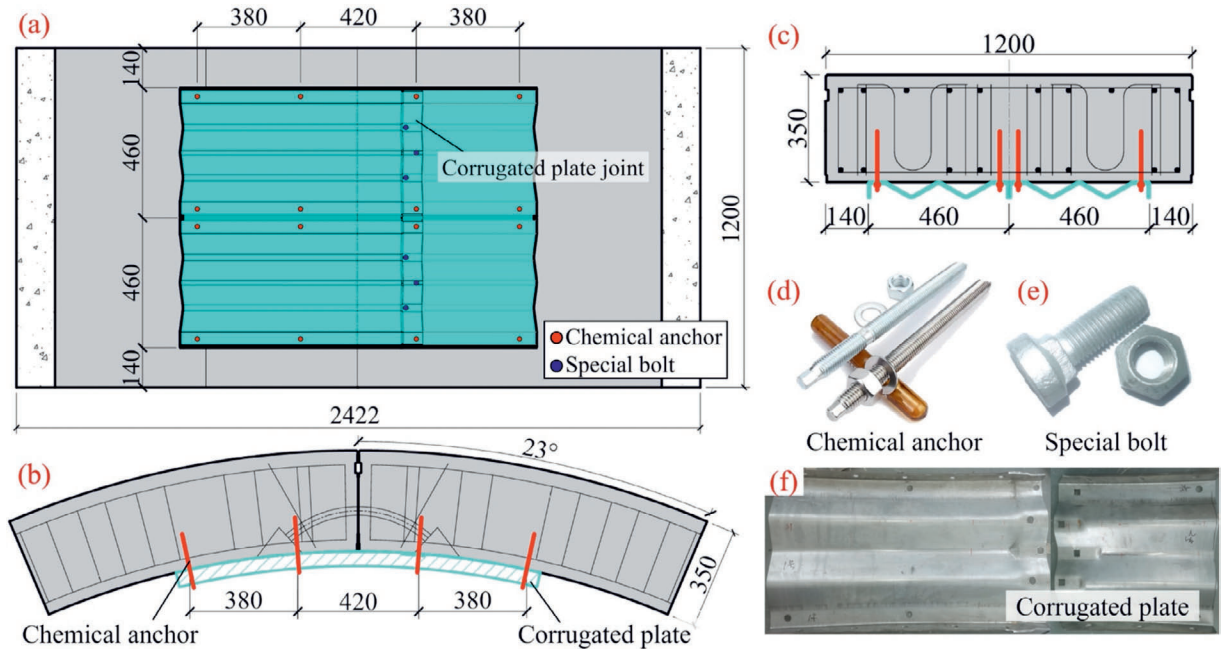

Fig. 1. Schematic diagram of the specimen SP-1. (a) Top view, (b) front view, (c) side view, (d) chemical anchor, (e) special bolt, and (f) corrugated plate. (Unit: mm)

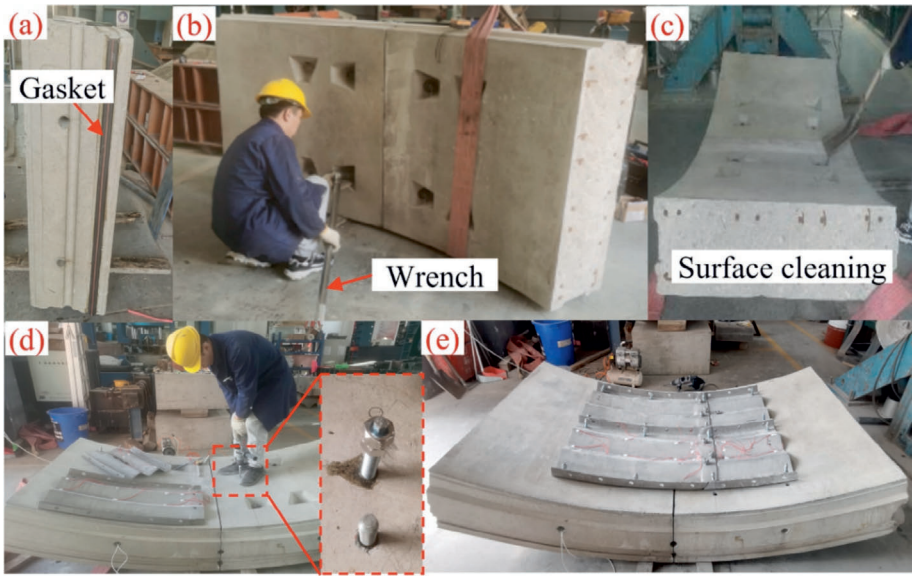

Fig. 2. Assembly process of the specimen SP-1.

equilibrium, Eq. (1) is derived to calculate the moment M at point A:

$$M = (F/2 + G) \times L - F/2 \times L_1 - G \times L_2 - N \times e, \quad (1)$$

where N, F, G, and M represent the axial load, vertical load, gravity of the segment and bending moment at point A, respectively; L, L_1, and L_2 denote the distances from the joint section to the vertical reaction force $F/2 + G$, the vertical load $F/2$, and the gravity G, respectively; e represents the eccentricity of the axial load N from point A.

To simulate the secondary loading condition, in which reinforcement is introduced only after damage has occurred, the reinforcement was not applied at the initial loading stage. According to the standard (China Society for the Promotion of Science and Technology Commercialization, 2021), the structural safety of the tunnel will be compromised when the joint opening reaches 4 mm, which was adopted as the reinforcement point. Upon reaching this point, the load was held steady, and reinforcement installation was completed by tightening the nuts on the anchors and bolts.

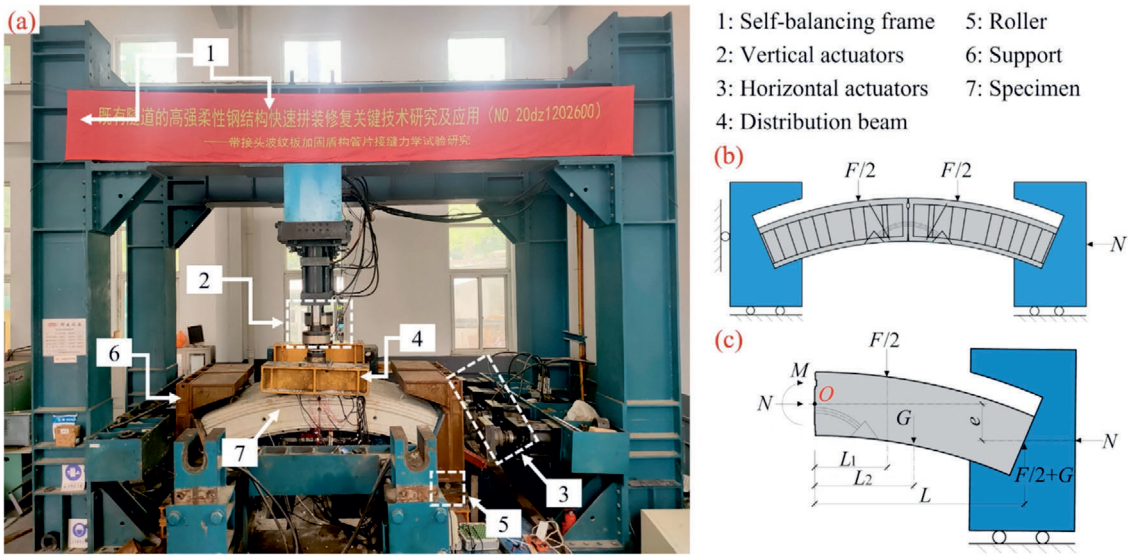

Fig. 3. Schematic diagram of (a) test apparatus, (b) load application, and (c) forces on the specimen.

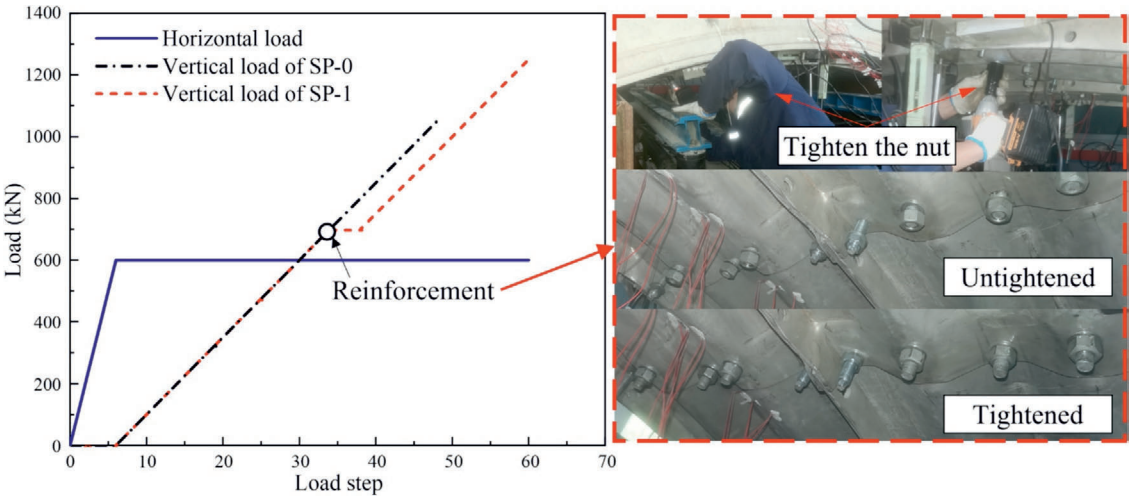

Fig. 4. Schematic diagram of test loading steps.

Table 1
Measurements for specimens.

Measuring item	Measurement instruments
Concrete strain	50 mm resistance strain gauge
Corrugated plate surface strain	3 mm resistance strain gauge
Bent bolt surface strain	3 mm resistance strain gauge
Segmental joint opening	100 mm tie rod displacement meter
Corrugated plate joint opening	100 mm tie rod displacement meter
Corrugated plate stripping	100 mm tie rod displacement meter
Segmental joint deflection	LXW pull-rope displacement meter
Crack width	Crack width tester mobile app

An axial force $N = 600$ kN was applied to the specimens, followed by vertical loading. The load increments for the axial and vertical directions were set to 100 kN and 25 kN per step, respectively. The schematic of the loading protocol and reinforcement procedure is demonstrated in Fig. 4.

2.3 Measuring program

The measurements in the tests are summarized in Table 1. Joint opening was recorded using four displacement transducers mounted on the extrados and intrados of the segment. Joint deflection was measured by four displacement transducers positioned on the intrados face. Concrete strain distribution along the height, width, and length of the joint was monitored with surface strain gauges. Strain gauges were applied to the upper and lower surfaces of the bent bolts to measure strain, with grooves incorporated to prevent compression of the gauges. Corrugated plate strain at crests and troughs was similarly measured with strain gauges. Stripping, defined as the distance between the extrados of the corrugated plate and the intrados of the segment, was recorded by two displacement transducers. Crack widths were measured with a mobile app. Data were logged using the DH3816N static test system.

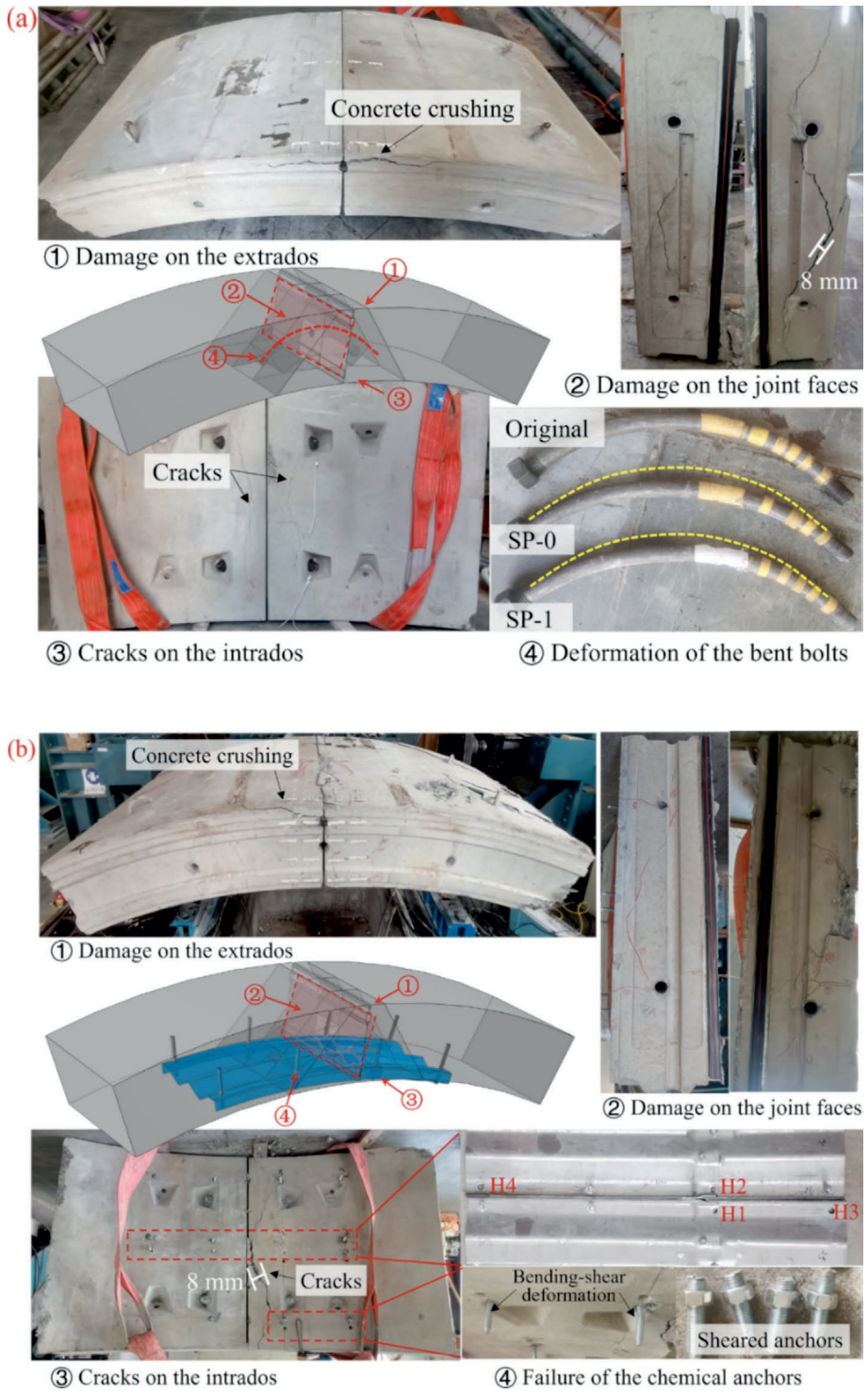

Fig. 5. Failure characteristics of the specimens. (a) SP-0, and (b) SP-1.

2.4 Result analysis

2.4.1 Failure mode

The failure mode of specimen SP-0 is shown in Fig. 5(a), where symmetrical crushing and spalling of concrete occurred on the extrados, accompanied by cracks on the intrados. Additionally, cracks with a maximum width of 8 mm developed along the joint face. The bent bolts showed significant tensile bending compared to original conditions, with more pronounced deformation observed in the bent bolts of SP-1.

The failure mode of the specimen SP-1 is depicted in Fig. 5(b). In the ultimate stage, the first failure observed was the shear fracture of the chemical anchors. Anchors H1 and H2 were the first to shear, transferring the shear force to the remaining anchors. This resulted in the shear-

ing of H3 and H4, ultimately leading to the disconnection between the corrugated plate and the segment. As a result, the strengthening effect of the corrugated plate was compromised. Subsequently, crushing of the concrete on the extrados occurred. According to Ding et al. (2023a), in the absence of a corrugated plate joint, specimen failure occurred due to concrete crushing. In this study, the presence of the corrugated plate joint resulted in uneven load distribution within the structure, causing localized stress concentration in chemical anchors, which leads to their failure prior to the concrete.

Meanwhile, in contrast to the symmetrical concrete crushing and cracking seen in SP-0, the specimen SP-1 exhibited asymmetric damage. On the side with the corrugated plate joint, the extrados of the concrete showed less severe damage, while the intrados and joint faces exhibited more significant cracking. The chemical anchors displayed considerable bending-shear deformation, and noticeable deformation was observed in the corresponding chemical anchor holes.

2.4.2 Vertical load-joint deflection

Figure 6 presents the vertical load-joint deflection relationships for both the unreinforced (SP-0) and reinforced (SP-1) specimens. These values were obtained by averaging measurements from corresponding points, with positive values indicating downward displacement. Under axial load, an eccentricity effect initially caused an upward deflection of approximately 8 mm. As the vertical load F gradually increased, the joint deflected progressively downward. At $F = 625$ kN, the intrados of the joint began to open. Following this, the bent bolts started to yield, resulting in a noticeable decrease in the slope of the curve. When $F = 825$ kN, contact occurred on the segment extrados face, restraining further vertical deformation and increasing the slope of the curve. At $F = 1000$ kN, a distinct crack developed on the joint's front surface. Finally, when F reached 1027 kN, the concrete reached its ultimate load-bearing capacity and failed due to crushing.

For specimen SP-1, the intrados joint opening reached 4 mm when the vertical load F was 700 kN, at which point reinforcement installation was initiated. After reinforcement, SP-1 exhibited reduced joint deflection compared to SP-0 under equivalent loads. At $F = 800$ kN, the joint deflections for SP-0 and SP-1 were 11.9 and 8.2 mm, respectively, showing a 31.1% reduction. At $F = 1000$ kN, the extrados face contacted. When F reached 1075 kN, cracks formed around the chemical anchors on the segments, and a noticeable gap developed at the corrugated plate joint. The chemical anchors were pulled, extracting fragments of resin. At $F = 1280$ kN, several chemical anchors sheared off, accompanied by localized concrete crushing and spalling, with a maximum deflection of 33.0 mm.

2.4.3 Moment-rotation angle relationship

Figure 7 shows the measurement method for the joint rotation angle, which is calculated with the joint opening at the intrados and extrados, following the Eq. (2).

$$\theta = 2\arctan\left(\frac{\delta_1 - \delta_2}{2h}\right), \tag{2}$$

where θ represents the rotation angle of the joint (rad); δ_1 and δ_2 denote the opening and closing displacements at the intrados and extrados of the joint (mm), respectively, openings are defined as positive, while closings are defined as negative; h denotes the thickness of the segment.

The moment-rotation angle relationships of SP-0 and SP-1 are presented in Fig. 8. Initially, both curves exhibit a similar linear growth trend until reaching the end of the full section closure (points A and a). It can be observed that the curves remain consistent prior to the reinforcement point (point R), indicating that the corrugated plate did not share the load during the early loading phase. After reinforcement, the curves of the two specimens begin to diverge. Under a moment of 200 kN·m, the rotation angles for SP-0 and SP-1 were 0.0485 and 0.0293 rad, respectively, representing a decrease of 39.6%. As the load increased, the extrados concrete contacted (points B and b), followed by concrete crushing (points C and c). Finally, the ultimate moments (points D and d) for SP-1 and SP-0 were 347.4 and 262.2 kN·m, respectively. The ultimate capacity of SP-1 is 32.5% higher than that of SP-0, demonstrating that the corrugated plate effectively enhances the bearing capacity and stiffness of the joint.

The flexural stiffness of the joint, representing its resistance to rotation under an applied moment, can be determined from the moment-rotation angle curves. The secant of the curve is used as an indicator of flexural stiffness and is calculated using Eq. (3).

$$K_\theta = \frac{\Delta M}{\Delta \theta}, \tag{3}$$

where K_θ denotes the flexural stiffness of the segmental joint, ΔM denotes the variation in moment, and $\Delta\theta$ denotes the variation in rotation angle.

Based on the variations in flexural stiffness, the loading process can be divided into four stages: (I) linear growth stage, (II) plastic development stage, (III) strengthening stage, and (IV) ultimate failure stage. Notably, the plastic development stage of the specimen SP-1 can be further divided into unreinforced (II_1) and reinforced (II_2) phases. The K_θ values for each phase of SP-0 and SP-1 are presented in Table 2. In stage I, the flexural stiffness of SP-0 is 18 773 (kN·m)/rad, while SP-1 exhibits a similar value of 18 500 (kN·m)/rad. Following reinforcement with the corrugated plate, the flexural stiffness in stage II for SP-1 increases to 3195 (kN·m)/rad, which is 38.4% higher than that of SP-0 (2309 (kN·m)/rad). Additionally, the flexural stiffness in stage III for SP-1 reaches 13 087 (kN·m)/rad, representing an increase of 112.4% compared to SP-0 (6162 (kN·m)/rad).

2.4.4 Bent bolt strain

The moment-strain relationship for the bent bolts is shown in Fig. 9, with tensile strain designated as positive.

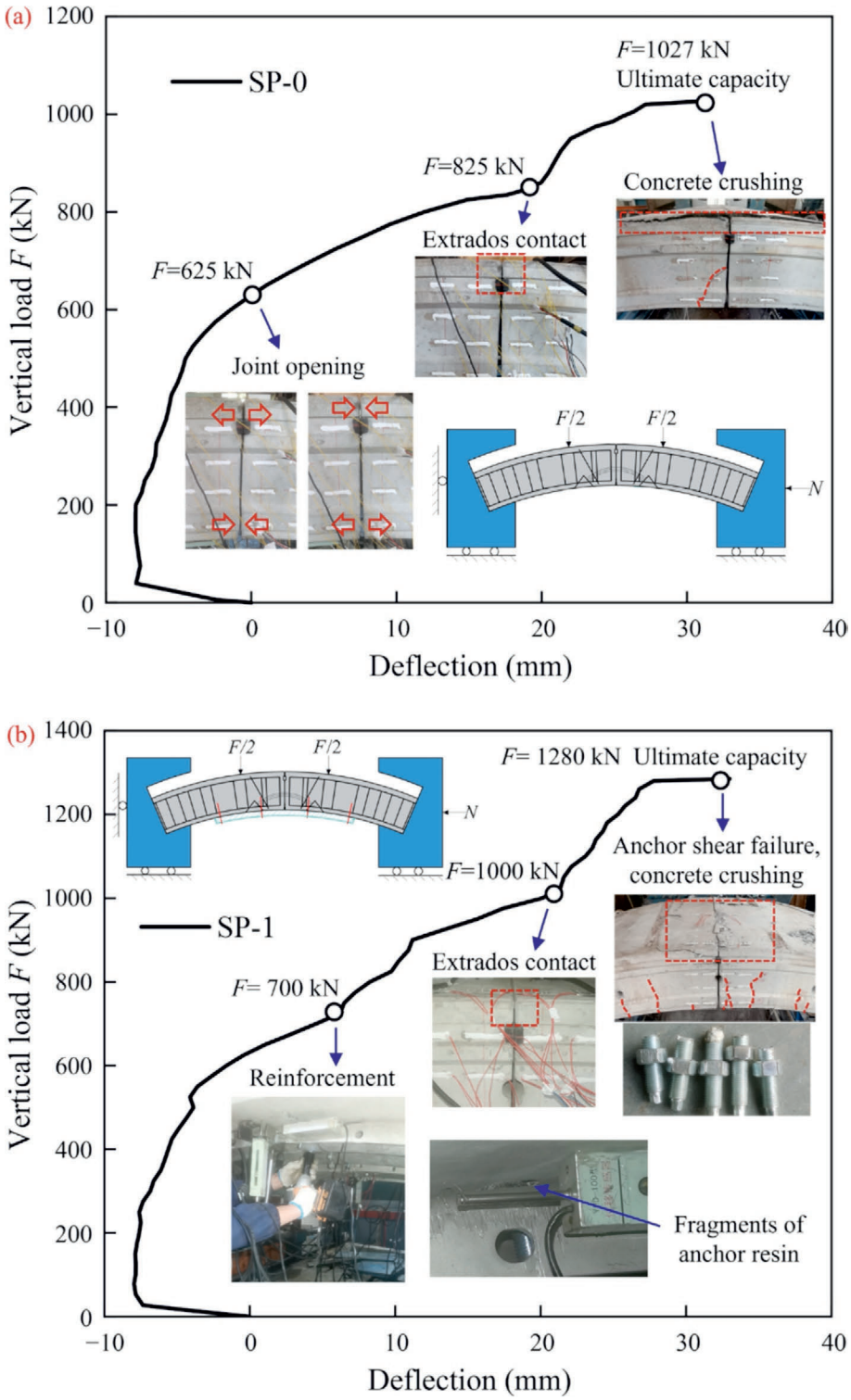

Fig. 6. Load-deflection relationships. (a) SP-0, and (b) SP-1.

Four strain gauges (T_1–T_4) were arranged at the mid-span of the bent bolts. For SP-0, as the load increased, the upper part of the bent bolt experienced compression while the lower part was in tension. In contrast, for SP-1, both the upper and lower parts of the bent bolts were subjected to tensile forces, and the strains were notably lower than those in SP-0. This indicates that the corrugated plate effectively redistributed the load from the bent bolts to the plate. When the moment reached 160 kN·m, both the upper and lower portions of the bent bolts in SP-0 yielded. At the point of ultimate failure, SP-0 reached a maximum compressive strain of 4396 με and a maximum tensile strain

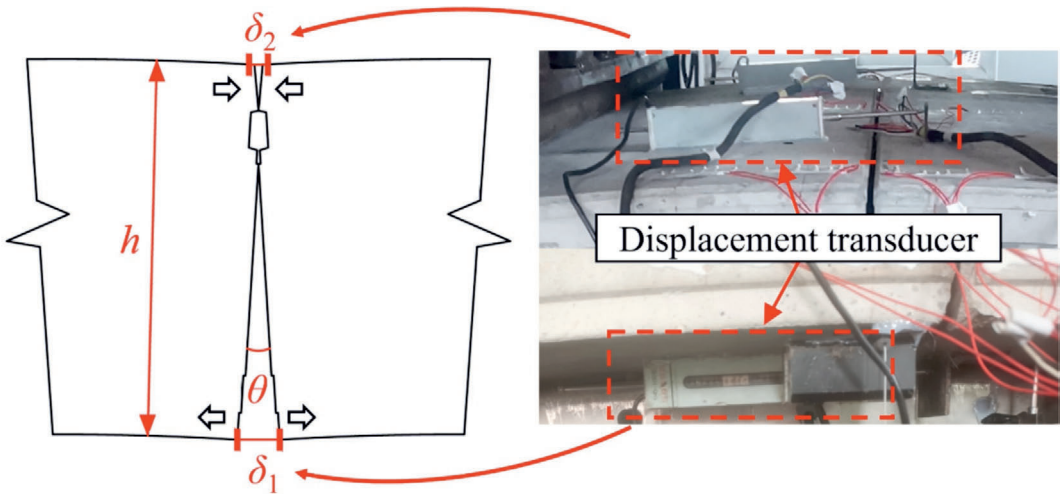

Fig. 7. Schematic diagram of the rotation angle of the segmental joint.

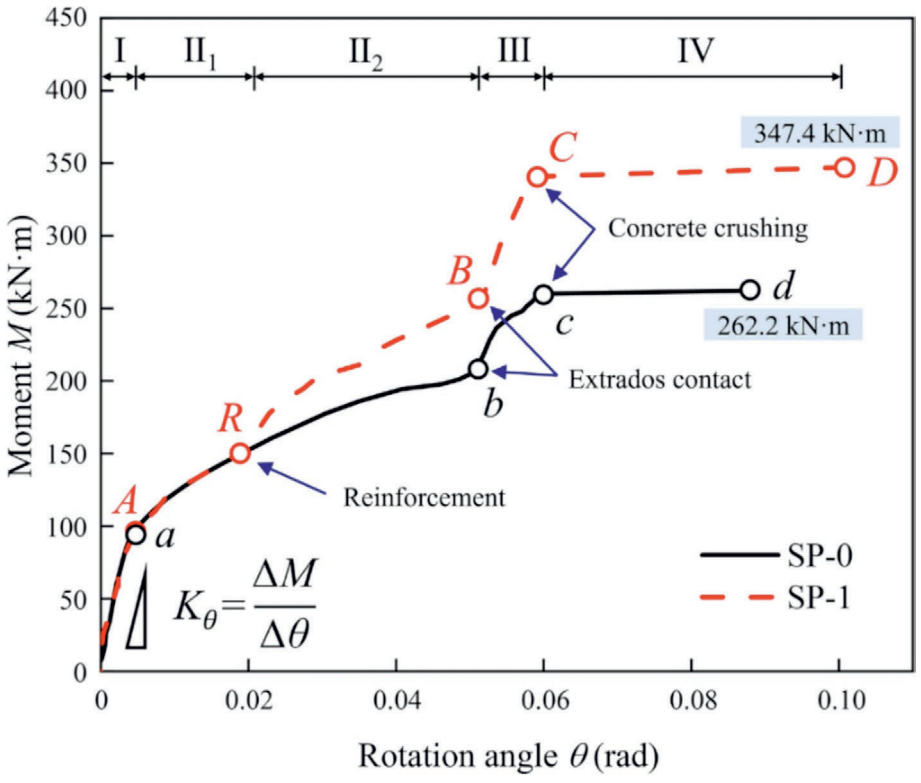

Fig. 8. Comparison of the moment-rotation angle relationship between SP-0 and SP-1.

Table 2
Comparison of flexural stiffness at different stages.

SP-0			SP-1			Improvement (%)
Stage	Moment (kN·m)	K_θ ((kN·m)/rad)	Stage	Moment (kN·m)	K_θ ((kN·m)/rad)	
I	0–102	18 773	I	0–102	18 500	
II	102–206	2309	II_1	102–152	2302	
			II_2	152–253	3195	38.4
III	206–260	6162	III	253–341	13 087	112.4
IV	260–262.2	82	IV	341.0–347.4	150	

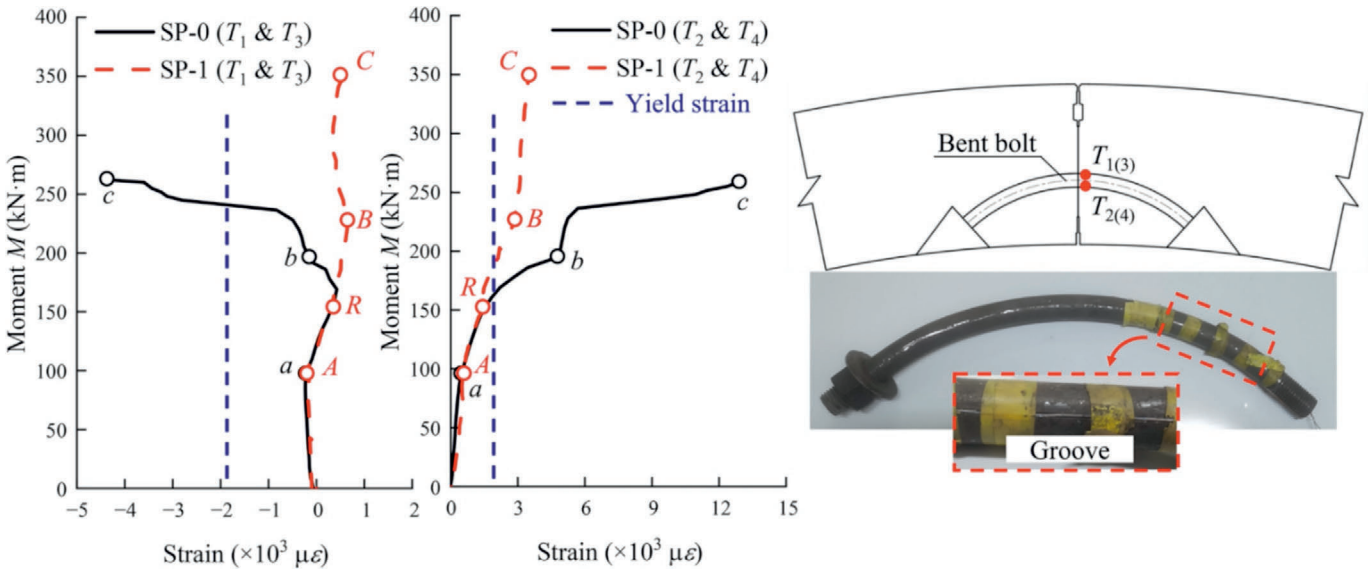

Fig. 9. Moment-bent bolt strain relationship of SP-0 and SP-1.

of 13 108 με, while SP-1 recorded maximum tensile strains of 527 and 3464 με, respectively. The bearing behavior of the bent bolts was significantly improved with the reinforcement.

2.4.5 Concrete strain

The concrete strain was assessed using strain gauges affixed to the surface of the segments. Data analysis indicated that the strain distribution across the segment width was more consistent and reliable than that along the segment thickness; therefore, only the widthwise strains are presented. Figure 10 illustrates the compressive strain development for SP-0 and SP-1, with negative values indicating compression. Initially, the concrete strains in both specimens were relatively low. As contact occurred at the extrados, the resulting contact force led to a gradual increase in concrete strain. The application of reinforcement significantly enhanced the flexural stiffness of the segmental joints and reduced joint opening. As a result, the contact at the extrados was delayed, improving the stress distribution within the concrete. The maximum compressive strains for SP-0 and SP-1 reached 973 and 1147 με, respectively.

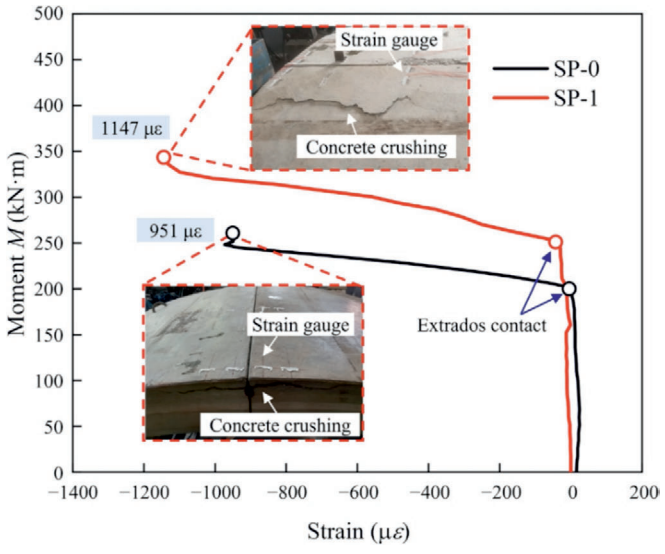

Fig. 10. Moment-concrete strain relationship of SP-0 and SP-1.

2.4.6 Corrugated plate strain

Figure 11 illustrates the strains at the crests (S1–S6) and troughs (S7–S12) of the corrugated plate, with tensile strain designated as positive. The results show that the crests of the corrugated plate were in compression, while the troughs were in tension. Following reinforcement, strain on the corrugated plate increased rapidly, indicating that the corrugated plate effectively shared the load. The maximum compressive and tensile strains were 768 and 1625 με, respectively, both remaining below the yield strain (0.2%), indicating that the plate was still within its elastic range and had not reached its ultimate strength. The maximum tensile and compressive strains were observed at the midspan. Strains on the corrugated plate showed slight asymmetry, with lower values on the side containing the corrugated plate joint. This is attributed to the fact that the stiffness of the joint is lower than that of the corrugated plate itself. As a result, the load was not uniformly distributed. Instead, it was concentrated more on the side without the joint, leading to higher strain levels.

2.4.7 Corrugated plate stripping and joint opening

The variations in corrugated plate stripping and joint opening are shown in Fig. 12. Here, deformation of the corrugated plate toward the segment and joint opening are taken as positive values. Prior to reinforcement, stripping values remained stable within a narrow range, and joint opening was essentially zero, indicating that the cor-

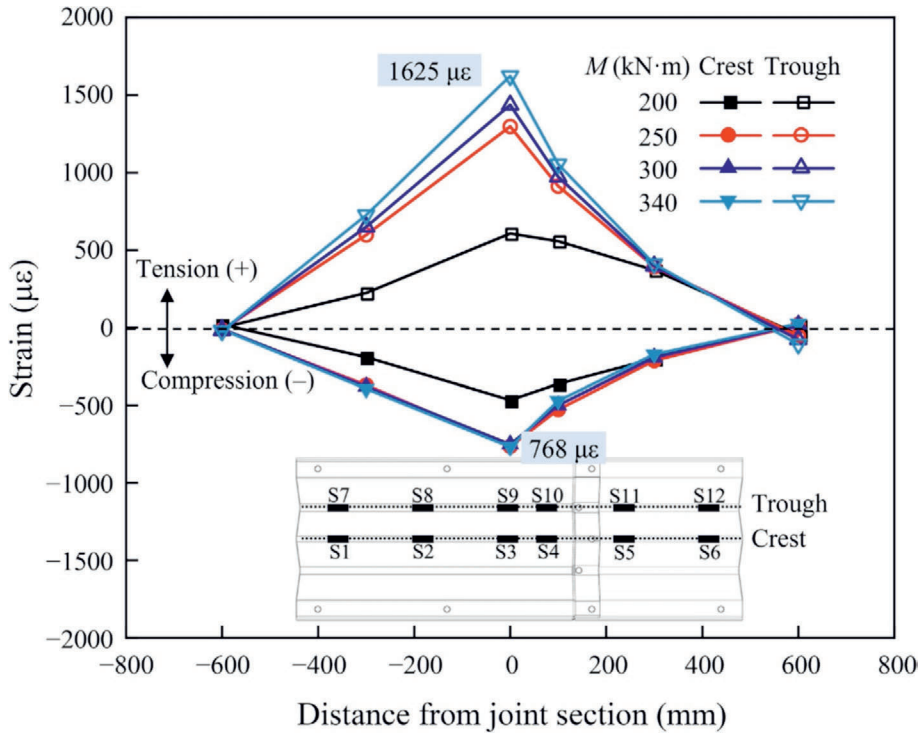

Fig. 11. Strain along the length of the corrugated plate for different moments.

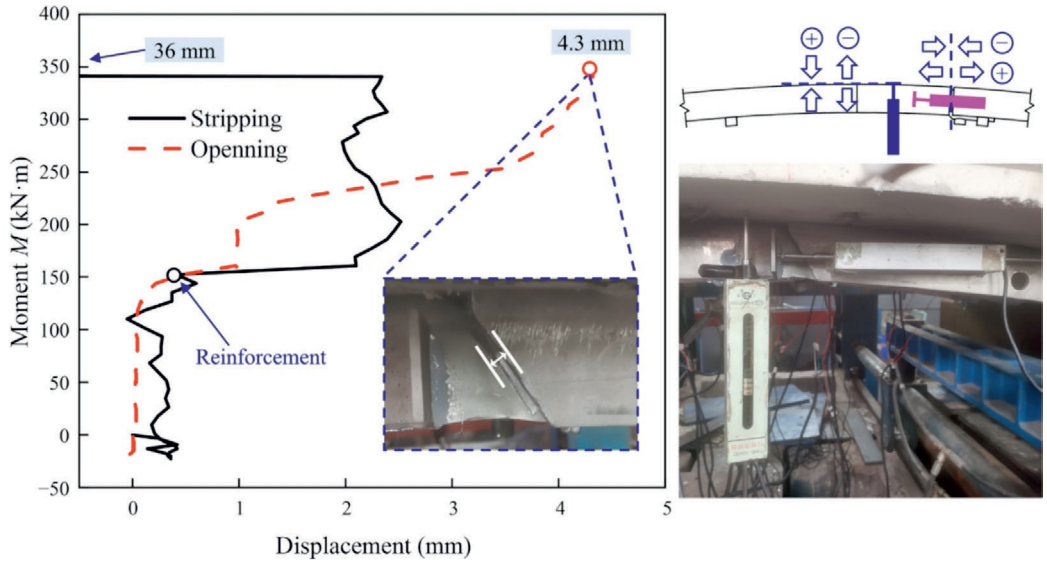

Fig. 12. Moment-stripping and moment-opening relationship of the corrugated plate joint.

rugated plate had not yet begun to share the load with the segment. Due to reinforcement installation, the corrugated plate moved 2 mm toward the segment, and the joint opened by approximately 1 mm. As the load increased, the stripping showed minimal change, demonstrating that the corrugated plate maintained a close fit with the segment. This reflected the effective collaborative bearing performance of the reinforced structure. The joint opening gradually increased, which was due to shear deformation occurring in the chemical anchors as the load was transferred from the segment to the corrugated plate. At the ultimate stage, the shear failure of several chemical anchors caused the corrugated plate to separate from the segment, with a maximum stripping of 36 mm and a joint opening of 4.3 mm.

3 Numerical study

Current research has primarily focused on joint-scale component reinforced with corrugated plates, with limited studies on full-ring reinforcement. In the following section, two numerical models for corrugated plate reinforcement

are developed using the finite element software ABAQUS at different scales: joint scale and full-ring scale. The joint-scale model was validated through comparison with experimental results, providing a reliable basis for the development of the full-ring model. The integration of these models enables a comprehensive investigation of the effectiveness of corrugated plate reinforcement.

3.1 Model establishment

3.1.1 Geometric modelling

Considering symmetry, a half-width model of the specimen was developed, with a width of 600 mm. The other dimensions of the joint-scale numerical model were consistent with those used in the specimen SP-1, as detailed in Section 2.1. The components of the model are illustrated in Fig. 13.

The geometry of the full-ring model was based on typical shield tunnel dimensions in Shanghai metro, with an outer diameter of 6200 mm, an inner diameter of 5500 mm, and a segment width of 1200 mm, as illustrated in Fig. 14(a). The whole lining consists of six pieces: three standard segments (A1, A2, A3), two adjacent segments (B1, B2), and one key segment (K), where K segment is wedge-shaped, and B1 and B2 segments also connect to the K segment with wedge shapes. Neighboring segments were connected by two bent bolts. The loads were applied to the segments through steel plates. The concrete used for the segments was C50 grade, while the bent bolts were 5.8 grade, with reinforcement cage grades of HPB300 and HRB400. This configuration matched that of the segmental joint test. For simplification, only longitudinal rebars were considered, excluding stirrups and hand hole rebars.

The configuration of the corrugated plate reinforcement is illustrated in Fig. 14(b), which consists of 14 corrugated plate segments (designated as CS1–CS14). This design aims to offset the joints of the corrugated plate from the segmental joints. The reinforcement structure consists of 14 corrugated plates (8 plates with a central angle of 18°, 2 plates with a central angle of 21°, and 4 plates with a central angle of 24°), along with two corbels and tie rods. The corrugated plates were made of S32001 stainless steel, measuring 460 mm in width and 6 mm in thickness. The corbels and tie rods were made from Q235 steel. The corbels are made up of steel plates with a thickness of 20 mm, and the tie rods featured cross-sectional dimensions of 80 mm × 20 mm. For each tunnel ring, two rings of corrugated plates were used for reinforcement. Since the effectiveness of corrugated plate reinforcement is significantly impacted by the shear capacity of the chemical anchors, the special bolts were substituted with chemical anchors to augment the connection between segments and corrugated plates.

3.1.2 Constitutive models of material

The mechanical behavior of C50 segmental concrete was modelled by a simplified Saenz constitutive model, as illustrated in Fig. 15(a). The C30 track bed was modelled with an elastic constitutive model, featuring an elastic modulus of 30 GPa and a Poisson's ratio of 0.2. The corrugated plate, made of S32001 stainless steel, followed the stress–strain relationship from (Li et al., 2022), as shown in Fig. 15(b). The yield strength of the corrugated plate was taken as the nominal yield strength corresponding to a 0.2% plastic strain, set at 517 MPa. The elastic modulus is 258 GPa, and the Poisson's ratio is 0.3.

Following the standards (Ministry of Housing and Urban-Rural Development of the People's Republic of China, 2015, 2017), the steel components were modelled using elastoplastic constitutive models, with material parameters summarized in Table 3. The plastic modulus for the steel was taken as 10% of the elastic modulus. The gasket was modeled using an elastic constitutive model, with an elastic modulus of 1 GPa and a Poisson's ratio of 0.45.

3.1.3 Element mesh and contact relationships

The rebars in the reinforcement cage were modelled using truss elements of type T3D2. All other components were modelled as solid elements, using linear hexahedral elements of type C3D8R. The mesh size of the components is listed in Table 4.

The interactions in the model are shown in Table 5. Surface-to-surface contact refers to the contact between two deformable surfaces or between a deformable surface and a rigid surface, where both normal and tangential behaviors should be defined. Hard contact was used to simulate the normal behavior, permitting separation while pre-

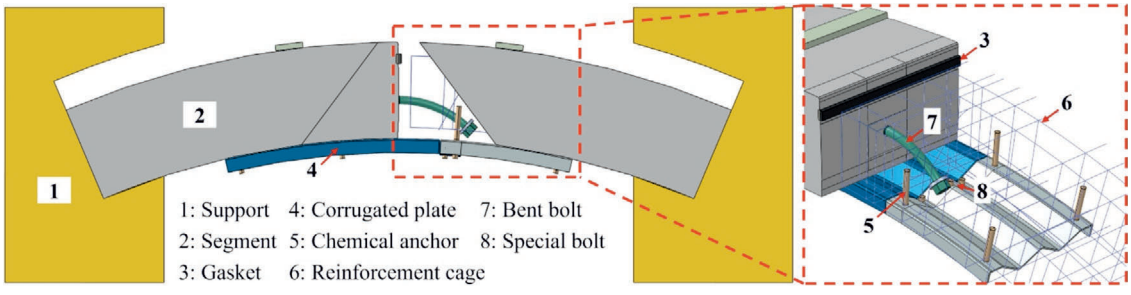

Fig. 13. Illustration of the joint-scale model.

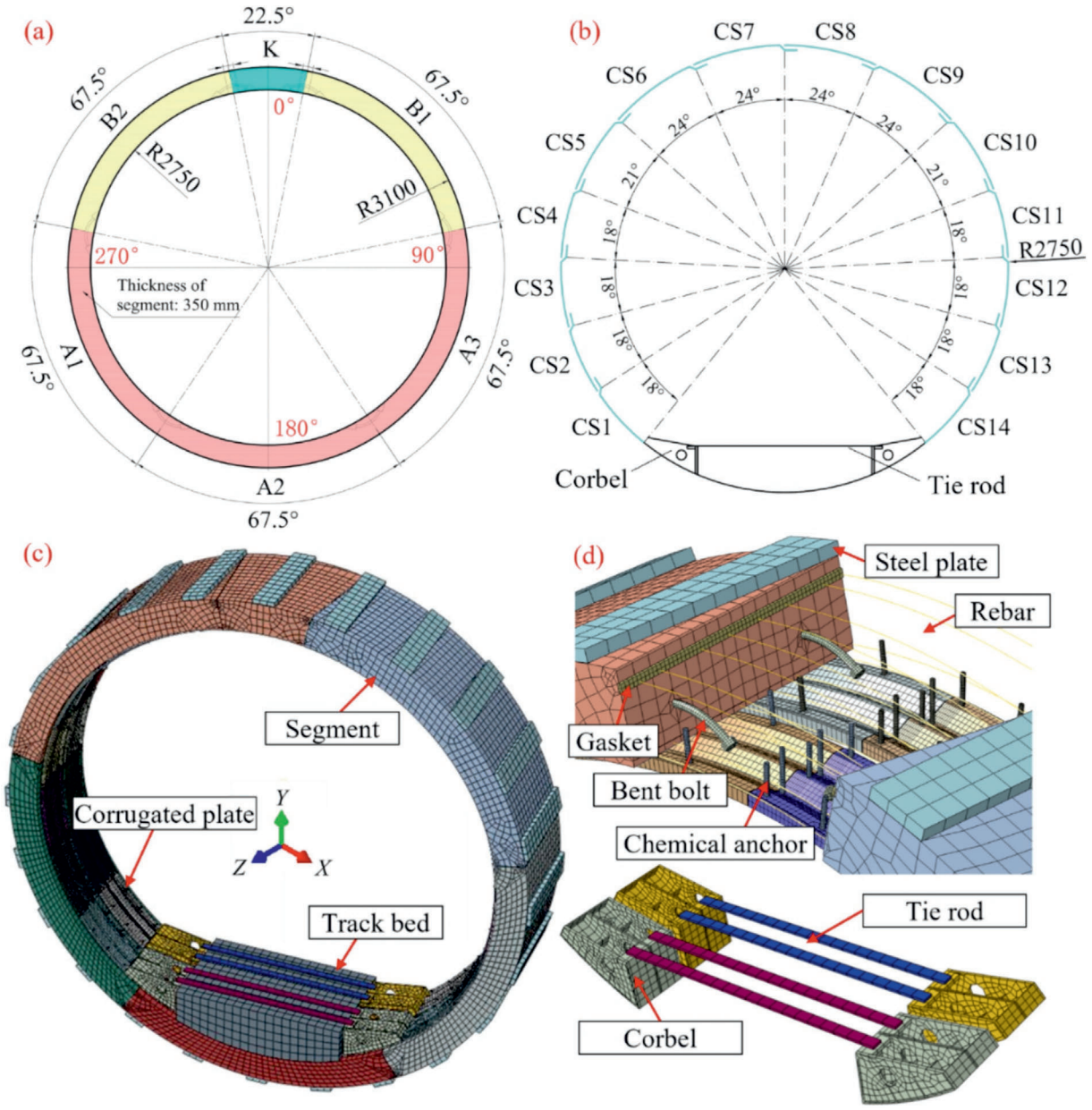

Fig. 14. Illustration of the full-ring scale model. (a) Geometric dimensions, (b) configuration of the corrugated plate reinforcement, (c) model establishment, and (d) components of the model. (Unit: mm)

venting penetration between adjacent components. Based on the Coulomb friction model, the tangential behavior was simulated by the penalty method with a specified friction coefficient, as listed in Table 6. Tie constraint simulates the perfect bond between the contact surfaces by equating all degrees of freedom between paired surfaces, including translational and rotational motions. Embedded region embedding a set of elements within another, and it is commonly used to simulate the bond interaction between reinforcement cage and segmental concrete. In all types of interactions, it is crucial to distinguish between the master and slave surfaces (Nassiraei, 2019, 2022). The larger of the two surfaces should act as the master surface. If the surfaces are of comparable size, the surface on the stiffer body and with the coarser mesh should act as the master surface (ABAQUS, 2016).

3.1.4 Load and boundary condition

The loading scheme for the joint-scale model aligned with that used in the tests, as detailed in Section 2.2. The loading protocol for the full-ring model followed the procedure established in the full-ring test (Liu et al., 2017). A total of 24 actuators were positioned around the tunnel lining at 15° intervals, with the loading positions divided into three groups, as shown in Fig. 16. The load magnitudes P_1, P_2, and P_3 were consistently controlled, with P_1 being greater than P_2 and P_3 to simulate top-overloading conditions.

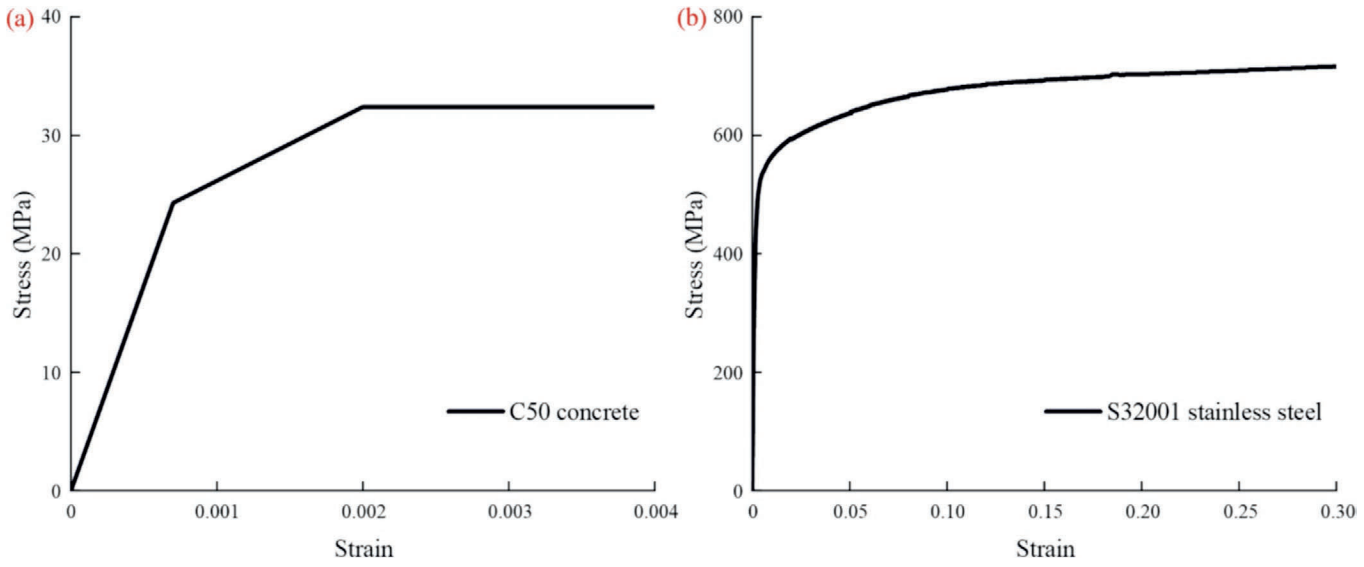

Fig. 15. Constitutive models of materials. (a) C50 concrete, and (b) S32001 stainless steel.

The loading was divided into three stages. In the first stage, P_2 increased from 0 to 275 kN, with $P_1 = 1.54P_2$ and $P_3 = 0.5(P_1 + P_2)$ to simulate the normal bearing state of the tunnel. In the second stage, while P_2 was held constant, P_1 was increased, with P_3 remaining at 0.5 $(P_1 + P_2)$, simulating an overloaded state. Loading continued until a vertical convergence ΔD of 120 mm was reached, marking the reinforcement point. In the third stage, following reinforcement, P_2 remained constant, and P_3 was held at $0.5(P_1 + P_2)$, and P_1 was increased until the ultimate bearing capacity was reached.

The boundary conditions of the models are illustrated in Fig. 17. For the joint-scale model, boundary conditions aligned with those used in the mechanical tests. The displacements along the *Y*-axis and *Z*-axis (U2 and U3), as well as the rotation around the *X*-axis and *Y*-axis (UR1 and UR2) of the supports, were prevented by setting the degrees of freedom of the bottom surface centerline to U2 = U3 = UR1 = UR2 = 0, and the displacement along the *X*-axis (U1) of the left support was also restricted (U1 = 0). For the full-ring model, considering the symmetry, the vault and invert, as well as the center of the track bed, were constrained along the *X*-axis and *Z*-axis (U1 = U3 = 0), the haunches were constrained along the *Y*-axis and *Z*-axis (U2 = U3 = 0). The boundary conditions of the models are illustrated in Fig. 17. For the joint-scale model, boundary conditions aligned with those used in the mechanical tests. The displacements along the *Y*-axis and *Z*-axis, as well as the rotation around the *X*-axis and *Y*-axis of the supports, were prevented by setting the degrees of freedom of the bottom surface centerline to U2 = U3 = UR1 = UR2 = 0, and the displacement along the *X*-axis of the left support was also restricted (U1 = 0). For the full-ring model, considering the symmetry, the vault and invert, as well as the center of the track bed, were constrained along the *X*-axis and *Z*-axis (U1 = U3 = 0), the haunches were constrained along the *Y*-axis and *Z*-axis (U2 = U3 = 0).

3.2 Numerical results

3.2.1 Model validation

In the numerical model, since components were modeled using elastoplastic constitutive models, structural failures such as anchors shearing off or concrete crushing were not explicitly simulated. Experimental observations indicated that shear failure of the chemical anchors was the primary cause of specimen failure. Therefore, the ultimate bearing capacity of the model was defined as the chemical anchors reaching an ultimate stress of 800 MPa. Figure 18 illustrates the results obtained from both the test and the model, showing that the numerical results are in good agreement with the experimental data. The model accurately reproduced the bending-shear deformation of the chemical anchors. In the ultimate state, the extrados of the concrete reached the ultimate compressive stress of 32.4 MPa, corresponding to the concrete crushing observed in the experiment. Comparisons of the ultimate moments showed values of 347.4 kN·m in the test and 368.8 kN·m in the simulation, with a difference of 6.2%, thereby verifying the validation of the proposed model.

To assess the rationality of the full-ring model, the numerical results were compared with the full-ring test (Liu et al., 2017). The model dimensions, concrete grades, and loading scheme of the simulation and test were identical, while the reinforcement used in the test was a steel plate instead of a corrugated plate. Therefore, the results before the reinforcement point were compared, as shown in Fig. 19. The numerical results align closely with the experimental data, with the reinforcement point corresponding to loads of 441.9 kN in the test and 432.6 kN in the simulation, differing by 2.1%. These results confirm

Table 3
Material parameters for steel components.

Component	Steel type	Elastic modulus (GPa)	Yield strength (MPa)	Yield strain	Ultimate strength (MPa)	Poisson's ratio
Reinforcement cage	HPB300 rebar	206	300	0.0014	420	0.3
	HRB400 rebar	206	400	0.0019	540	0.3
Bent bolts and washers	Grade 5.8 carbon steel	206	400	0.0019	500	0.3
Supports and plates	Q235	206				0.3
Corbels and tie bars	Q235	206	235	0.0011	375	0.3
Chemical anchors	Grade 8.8 2205 stainless steel	206	640	0.0031	800	0.3
Special bolts	Grade 10.9 high-strength steel	206	900	0.0044	1000	0.3

Table 4
Mesh size of the components.

Component	Segment	Rebar	Bent bolt	Steel plate	Gasket	Corbel	Tie rod	Corrugated plate	Chemical anchor
Mesh size (mm)	80	40	10	100	20	60	60	25	10

Table 5
Contact pairs of interactions.

Contact pair	Surfaces		Interaction
	Master	Slave	
Segment-segment	Segment	Segment	Surface-to-surface
Segment-bent bolt	Segment	Bent bolt	Surface-to-surface
Corrugated plate-corrugated plate	Corrugated plate	Corrugated plate	Surface-to-surface
Segment-corrugated plate	Segment	Corrugated plate	Surface-to-surface
Segment-corbel	Segment	Corbel	Surface-to-surface
Segment-track bed	Track bed	Segment	Surface-to-surface
Gasket-gasket	Gasket	Gasket	Surface-to-surface
Corbel-track bed	Track bed	Corbel	Surface-to-surface
Segment-gasket	Segment	Gasket	Tie
Segment-steel support	Segment	Steel support	Tie
Segment-bent bolt washer	Segment	Bent bolt washer	Tie
Bent bolt nut-bent bolt washer	Bent bolt nut	Bent bolt washer	Tie
Corrugated plate-chemical anchor	Corrugated plate	Chemical anchor	Tie
Corrugated plate-special bolt	Corrugated plate	Special bolt	Tie
Corrugated plate-corbel	Corbel	Corrugated plate	Tie
Corbel-tie rod	Corbel	Tie rod	Tie
Segment-reinforcement cage			Embedded region
Segment-chemical anchor			Embedded region

the suitability of the established model for investigating the full-ring reinforcement effects of corrugated plates.

In the ultimate state, the tunnel presents an elliptical deformation: the vault contracted inward, while the haunches expanded outward. Comparing the P_1-vertical convergence curves for the unreinforced and the reinforced conditions, it is observed that the ultimate load P_1 of the unreinforced tunnel is 447.2 kN, corresponding to a maximum convergence of 229.6 mm. Following reinforcement with corrugated plates, the stiffness increased from 469.2 kN/m to 2071.0 kN/m, an increase of 341.4%. The ultimate load P_1 increased to 624.5 kN, reflecting a 39.6% improvement compared to the unreinforced condition.

3.2.2 Joint opening

Figure 20 shows the variation in joint openings at different loading stages. Considering the symmetry of the structure and load, only half of the tunnel is analyzed. Positive moments correspond to those causing compression in the

Table 6
Tangential friction coefficient of contact pairs.

Contact pair	Tangential friction coefficient
Concrete-concrete	0.6
Concrete-steel	0.3
Steel-steel	0.1
Gasket-gasket	0.6

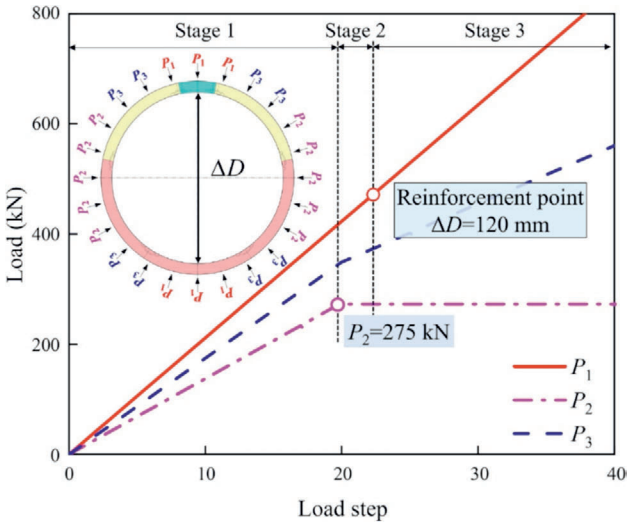

Fig. 16. Loading scheme of the full-ring scale model.

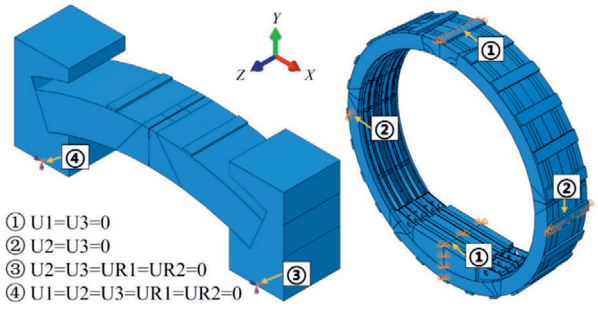

Fig. 17. Schematic illustration of boundary conditions.

extrados and tension in the intrados of the tunnel. Joints 1# and 3# are located in the positive moment region, while Joint 2# lies in the negative moment region. When P_1 reached 624.5 kN, the intrados openings of Joints 1# and 3# were 16.3 mm and 12.3 mm, respectively, while the extrados opening of Joint 2# was 34.5 mm. Joint 2# exhibited the largest opening because it experienced a larger bending moment, and the flexural stiffness under negative moments is generally lower than under positive moments.

3.2.3 Stress distribution

Figure 21 illustrates the von Mises stress distribution within the tunnel segments. Notably, high stress levels

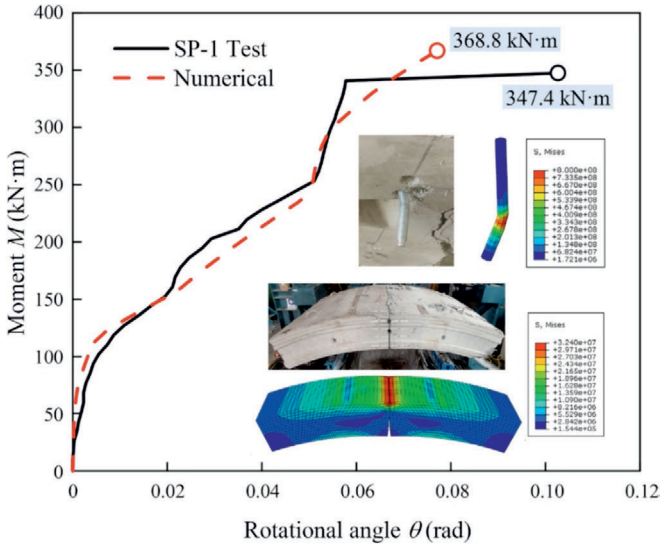

Fig. 18. Moment-rotation angle relationship obtained from the test and joint-scale model.

occur at the concrete contact faces along the segmental joints, reaching the ultimate strength of 32.4 MPa. Significant stress was observed in the tunnel segments at the vault, haunch, and invert, where the joint experienced higher bending moments. Stress concentration was especially pronounced near the key segment, attributed to its unique wedged shape and weaker stiffness (Zhang et al., 2022). Furthermore, stress concentrations were also evident around the hand holes for the bent bolts.

Figure 22 shows the stress distribution in the corrugated plates, with high stress concentrated at the vault and haunch, and the maximum stress (688.3 MPa) occurred near the chemical anchor holes at the vault. The stress distribution in the corrugated plates was similar to that in the segments, demonstrating the collaborative bearing behavior of the corrugated plates and segments. Additionally, elevated stress was observed at the connection between the corrugated plates and corbels, emphasizing the importance of high-quality welding at these junctions. The chemical anchors primarily experienced shear forces, with those at the vault reaching an ultimate stress of 800 MPa, while the anchors at the haunch showed a maximum stress of 650.6 MPa. Due to the joint opening at these locations, the chemical anchors underwent increased shear deformation to facilitate coordinated deformation between the segments and the corrugated plates, leading to elevated shear stress. Therefore, the configuration of the chemical anchors could be optimized in these areas, for instance, by increasing the number of anchor rows.

4 Conclusions

In this paper, the mechanical characteristic of segmental joints reinforced with corrugated plates was investigated, and the overall and local responses of specimens were compared. Two scales of numerical models were established

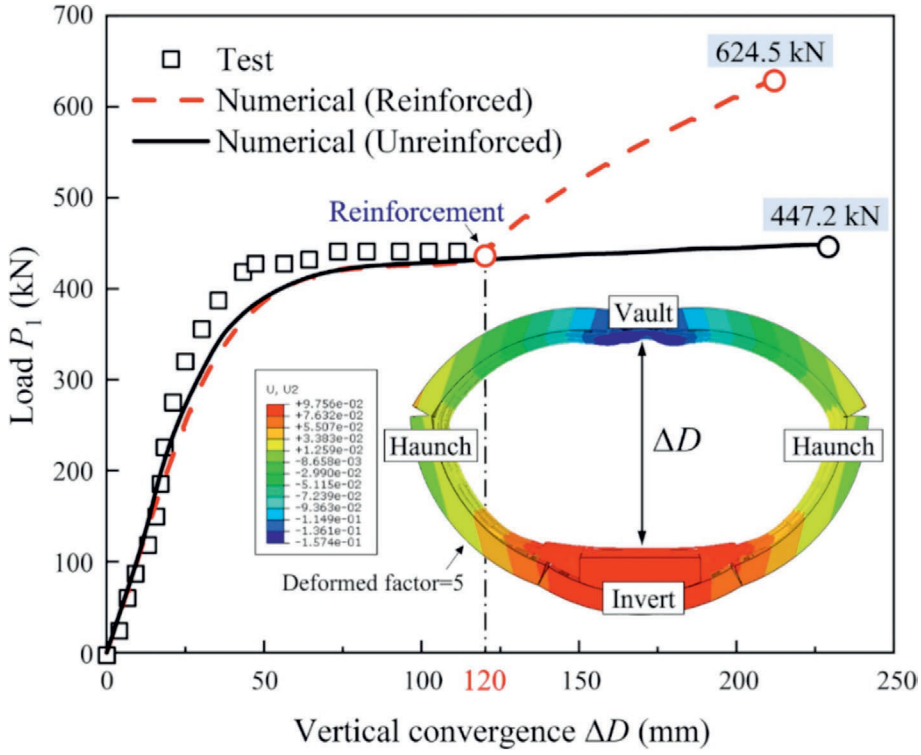

Fig. 19. Load P_1-vertical convergence relationship obtained from the test and full-ring scale model.

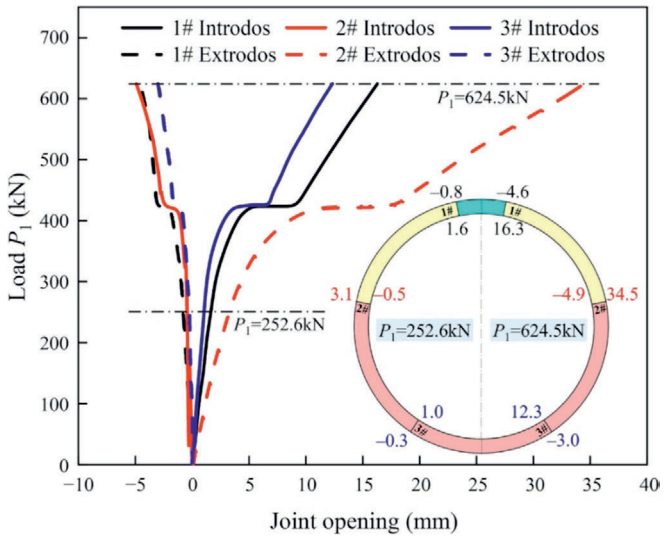

Fig. 20. Load P_1-joint opening relationship.

and validated, and the effectiveness of the corrugated plate reinforcement on shield tunnels was comprehensively analyzed. The main conclusions are as follows:

(1) The corrugated plate joint caused uneven load distribution in the specimen, resulting in an asymmetric extent of damage. The failure mode was characterized by the shear failure of the chemical anchors, followed by concrete crushing. The effectiveness of reinforcement highly depends on the shear capacity of the chemical anchors.

(2) The loading process can be divided into four stages: (I) linear growth stage, (II) plastic development stage, (III) strengthening stage, and (IV) ultimate failure stage. Compared to the unreinforced specimen, the ultimate moment of the reinforced specimen increased by 32.5%, with flexural stiffness improving 38.4% in stage II and 112.4% in stage III.

(3) There was minimal stripping between the corrugated plates and the segments before failure, demonstrating effective collaborative bearing performance. Due to its high strength, the corrugated plate remained in an elastic state at the time of failure, suggesting that the bearing capacity of the corrugated plate could be further utilized by optimizing the anchor arrangement.

(4) With full-ring reinforcement, the tunnel stiffness increased from 469.2 kN/m to 2071.0 kN/m, reflecting a 341.4% increase, and the bearing capacity rose from 447.2 kN to 624.5 kN, representing an improvement of 39.6%. Stresses in the segments and corrugated plates were concentrated at the tunnel vault and haunch, where chemical anchors experienced elevated shear stress. Therefore, local densification of chemical anchors is recommended in these regions. Additionally, the connection between the corrugated plates and the corbels should also be given careful consideration.

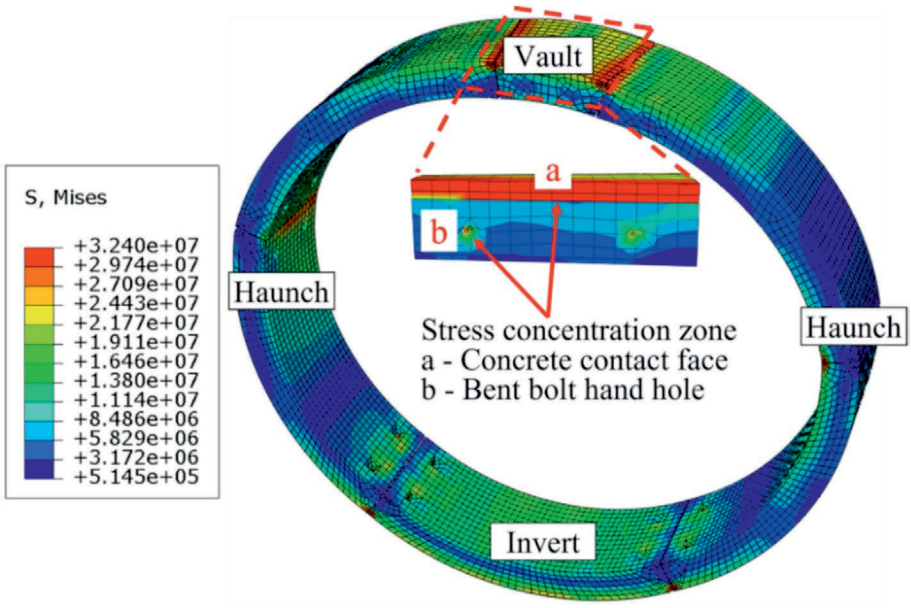

Fig. 21. Simulated results of stress distribution of segments.

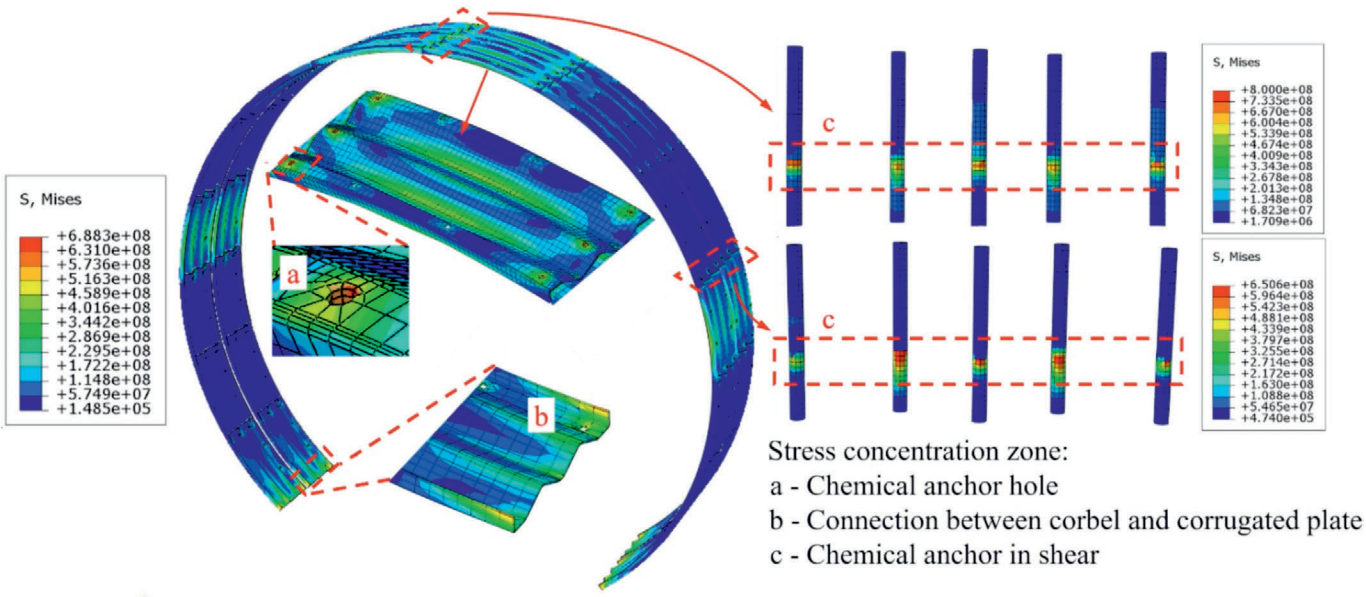

Fig. 22. Simulated results of stress distribution of corrugated plates and chemical anchors.

Data availability

The data that support the findings of this study are available from the corresponding author upon reasonable request.

CRediT authorship contribution statement

Yingjie Guo: Formal analysis, Methodology, Software. **Wenqi Ding:** Supervision, Conceptualization, Funding acquisition. **Chang Ma:** Writing – original draft, Investigation. **Jixiang Tang:** Writing – review & editing, Validation. **Qingzhao Zhang:** Resources.

Declaration of competing interest

The authors declare that they have no known competing financial interests or personal relationships that could have appeared to influence the work reported in this paper.

Acknowledgement

This study was supported by the National Natural Science Foundation of China (Grant Nos. 52378405 and 52090083) and the Major Science and Technology Project of the Yunnan Department of Transportation (Grant No. 202302AD080007).

References

ABAQUS (2016). *ABAQUS Documentation. Dassault Syste´mes*. Paris, France: Ve´lizy-Villacoublay.

Arnau, O., & Molins, C. (2012). Three dimensional structural response of segmental tunnel linings. *Engineering Structures, 44*, 210–221.

Cao, Y., Wang, P. Y., Jin, X. L., Wang, J. W., & Yang, Y. Z. (2012). Tunnel structure analysis using the multi-scale modeling method. *Tunnelling and Underground Space Technology, 28*, 124–134.

Chang, C. T., Wang, M. J., Chang, C. T., & Sun, C. W. (2001). Repair of displaced shield tunnel of the Taipei rapid transit system. *Tunnelling and Underground Space Technology, 16*(3), 167–173.

China Society for the Promotion of Science and Technology Commercialization. (2021). T/CSPSTC 68—2021: *Technical code of practice for structural repair and reinforcement of metro shield tunnels.* China Architecture & Building Press, Beijing, China (in Chinese).

Ding, W. Q., Guo, Y. J., Li, S. B., Li, X. R., & Zhang, Q. Z. (2023a). Experimental research on the mechanical behavior of segmental joints of shield tunnel reinforced with a new stainless steel corrugated plate. *Case Studies in Construction Materials, 18*, e02170.

Ding, W. Q., Ma, C., Guo, Y. J., Li, X. R., & Li, S. B. (2023b). Numerical analysis of new stainless-steel corrugated-plate reinforcement of shield-tunnel segmental joints based on virtual-tracking-element technology. *Applied Sciences, 13*(10), 5904.

Do, N. A., Dias, D., Oreste, P., & Djeran-Maigre, I. (2014). Three-dimensional numerical simulation for mechanized tunnelling in soft ground: The influence of the joint pattern. *Acta Geotechnica, 9*(4), 673–694.

Kang, J. S., & Davidson, J. S. (2013). Structural effects of concrete lining for concrete-lined corrugated steel pipes. *Structure and Infrastructure Engineering, 9*(2), 130–140.

Li, H. Y., Li, X. G., & Liu, H. (2023). Deformation and failure mechanism of metro shield tunnel subjected to buried fault dislocation. *Engineering Failure Analysis, 153*, 107551.

Li, S. B., Ding, W. Q., Zhang, Q. Z., Xiao, X. Y., & Zhou, Q. L. (2022). Experimental study of the mechanical properties of a new duplex stainless steel exposed to elevated temperatures. *Case Studies in Construction Materials, 17*, e01683.

Liu, X., Jiang, Z. J., & Zhang, L. L. (2017). Experimental investigation of the ultimate bearing capacity of deformed segmental tunnel linings strengthened by epoxy-bonded filament wound profiles. *Structure and Infrastructure Engineering, 13*(10), 1268–1283.

Liu, X., Jiang, Z. J., Yuan, Y., & Mang, H. A. (2018). Experimental investigation of the ultimate bearing capacity of deformed segmental tunnel linings strengthened by epoxy-bonded steel plates. *Structure and Infrastructure Engineering, 14*(6), 685–700.

Liu, X. Z., Sang, Y. L., Ding, S., You, G. L., Zhu, W. X., Zhou, R. Y., Wei, Q., & Jiang, L. (2020). Experimental study on the mechanics characteristics of CFRP strengthening of highway tunnels at different damage states. *Geofluids, 2020*, 6665996.

Ma, C., Ding, W. Q., Zhang, Q. Z., & Huang, X. B. (2024). Mechanical characteristics of flange joints for corrugated steel plate: Experiment and simulation. *Journal of Constructional Steel Research, 221*, 108919.

Mikhailovsky, L., Laurie Kennedy, D. J., & Lee, R. W. S. (1992). Flexural behaviour of bolted joints of corrugated steel plates. *Canadian Journal of Civil Engineering, 19*(5), 896–905.

Ministry of Housing and Urban-Rural Development of the People's Republic of China. (2015). GB 50010—2010: *Code for design of concrete structures*. China Architecture & Building Press, Beijing, China (in Chinese).

Ministry of Housing and Urban-Rural Development of the People's Republic of China. (2017). GB 50017—2017: *Standard for design of steel structures*. China Architecture & Building Press, Beijing, China (in Chinese).

Nassiraei, H. (2019). Local joint flexibility of CHS X-joints reinforced with collar plates in jacket structures subjected to axial load. *Applied Ocean Research, 93*, 101961.

Nassiraei, H. (2022). Geometrical effects on the LJF of tubular T/Y-joints with doubler plate in offshore wind turbines. *Ships and Offshore Structures, 17*(3), 481–491.

Rauch, A. F., Sargand, S. M., & Hazen, G. A. (1994). Behavior of deeply corrugated steel plate in culvert. *Journal of Structural Engineering, 120*(5), 1651–1655.

Ren, T. Y., Liu, S. Y., & Liu, X. (2019). Experimental study of bending capacity of shield tunnel lining segment strengthened by corrugated steel. *Tunnel Construction, 39*(2), 317–323 (in Chinese).

Su, D., Chen, W. J., Wang, X. T., Huang, M. L., Pang, X. C., & General, X. S. (2022). Numerical study on transverse deformation characteristics of shield tunnel subject to local soil loosening. *Underground Space, 7*(1), 106–121.

Tetreault, J., Hoult, N. A., & Moore, I. D. (2018). Pre- and post-rehabilitation behaviour of a deteriorated horizontal ellipse culvert. *Canadian Geotechnical Journal, 55*(3), 329–342.

Wu, Y. D., Ding, W. Q., Li, S. B., & Qiao, Y. F. (2023). Effect of oblique bolt arrangement on flexural behavior of segmental joint for shield tunnel. *Tunnelling and Underground Space Technology, 135*, 105043.

Yuan, Y., Jiang, X. M., & Liu, X. (2013). Predictive maintenance of shield tunnels. *Tunnelling and Underground Space Technology, 38*, 69–86.

Zahran, E. H. (2016). Studying the behavior of strengthened four shapes of RC tunnels using externally bonded GFRP. *International Journal of Engineering and Applied Sciences, 3*(3), 11–14.

Zhai, W. Z., Chapman, D., Zhang, D. M., & Huang, H. W. (2020). Experimental study on the effectiveness of strengthening over-deformed segmental tunnel lining by steel plates. *Tunnelling and Underground Space Technology, 104*, 103530.

Zhang, J. L., Liu, X., Ren, T. Y., Yuan, Y., & Mang, H. A. (2019). Structural behavior of reinforced concrete segments of tunnel linings strengthened by a steel-concrete composite. *Composites Part B: Engineering, 178*, 107444.

Zhang, W. J., Qi, J. B., Zhang, G. L., Niu, R. J., Zhang, C., He, L. C., & Lyu, J. R. (2022). Full-scale experimental study on failure characteristics of the key segment in shield tunnel with super-large cross-section. *Tunnelling and Underground Space Technology, 129*, 104671.

Zhao, G. Q., Liu, J. T., Meng, S. Y., Liu, C. Y., & Wang, Q. H. (2023). Performance of corrugated steel plate flange joint under combined compression and Bending: Experimental and numerical investigations. *Construction and Building Materials, 389*, 131798.